SHocks: structure, AcceleRation, dissiPation

Work Package 2
Structure of heliospheric shocks

Deliverable D2.3
Technical report on the observational evidence of shock variability

Andrew P. Dimmock[1], Yuri Khotyaintsev[1], Ahmad Lalti[1], Andreas Johlander[1], Daniel Graham[1], Michael Gedalin[2]

[1] Swedish Institute of Space Physics, Uppsala, Sweden, [2] Finnish Meteorological Institute, Helsinki, Finland

29/09/2022

This project has received funding from the European Union's Horizon 2020 research and innovation programme under grant agreement No 101004131

Document Change Record

Issue	Date	Author	Details
1.0	27/09/2022	A. P. Dimmock	Shared with co-authors
2.0	29/09/2022	A. P. Dimmock	Revised and submitted after co-author comments

Table of Contents

1 Summary

This technical report provides an overview of the studies on the topic of shock variability using observations. Here, shock variability refers explicitly to the time-dependent nature of the shock front, which includes waves, instabilities, and forms of nonstationarity such as rippling, and reformation.

2 Introduction

Shock waves appear in a wide variety of space plasmas where they act to slow down and heat supersonic flows before the plasma can encounter an obstacle. Plasma shocks in the heliosphere and astrophysical settings are often collisionless, meaning that heating and entropy generation takes place through interactions between the particles and the electromagnetic fields. However, the behaviour of the particles (ions and electrons) is dictated by the shock structure, which itself is highly variable. This variability can be connected to numerous mechanisms such as the variable speed of the shock ramp, waves and instabilities, shock rippling, and reformation. All of these are also sensitively coupled to the parameter regime of the shock such as Mach number and geometry.

We have investigated numerous forms of shock variability, to advance the knowledge of how ions and electrons behave across the shock during these dynamic regimes. This behaviour has been studied by Johlander et al. [2022, submitted] (appended to this report) and investigates the electron temperature profile across the shock front while connecting it to the shock ramp speed. The study by Dimmock et al. [2022] analyses the Venus bow shock and presents whistler waves at different frequency bands. In addition, the shock shows clear signatures of nonstationarity such as large density and magnetic field changes inside the ramp. Later, we present work that connects shock variability to the heating of electrons, and at what spatial scale this heating takes place. We then introduce an automated method to identify nonstationary shocks to study such shocks statistically. Finally, Lalti et al. [2022] investigates the generation of whistler waves in the shock foot. These studies are described in the following text and Johlander et al. [2022, submitted] is included after this report.

3 Observational evidence of shock variability

3.1 Electron heating scales at quasi-perpendicular shocks

Electron heating at collisionless shocks in space is a combination of adiabatic heating due to large-scale electric and magnetic fields and non-adiabatic scattering by high-frequency fluctuations. The scales at which heating happens can hint at what physical processes are taking place. Here, we study electron heating scales with data from the Magnetospheric Multiscale (MMS) spacecraft at Earth's quasi-perpendicular bow shock. An overview of one of the elected events, named Event 1, observed by MMS1 is shown in Figure 1A-C. The shock ramp is seen as a sharp boundary in number density N and electron temperatures. The parallel and perpendicular temperatures are similar in the ramp and downstream of the shock with temperature anisotropy close to 1. The temperature profile in panel (Ac)

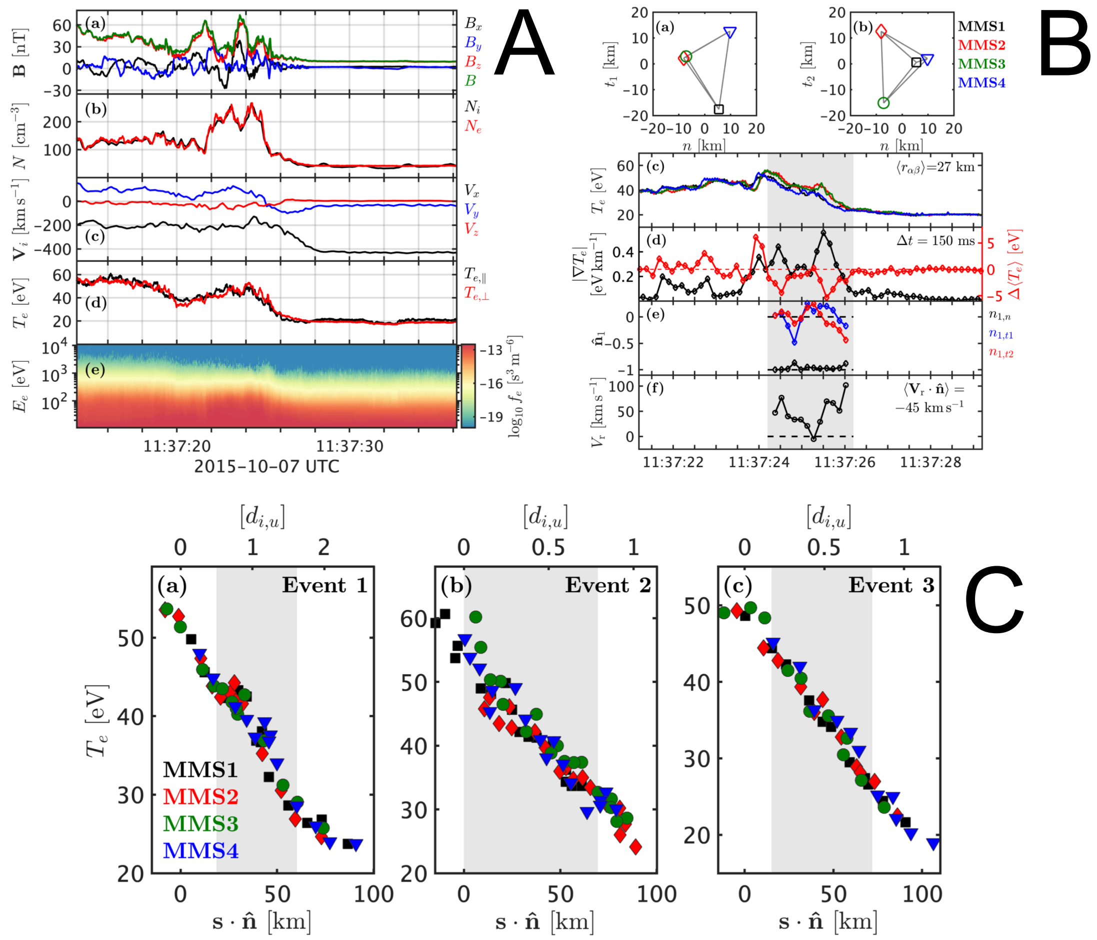

Figure 1: Panels (A) show a Shock crossing by MMS1. (a) Magnetic field B in GSE coordinates. (b) Ion and electron number densities Ni,e. Ion flow velocity Vi. (e) omnidirectional electron phase-space density as a function of energy. Panels (B) present a shock crossing seen by the four spacecraft (see Johlander et al. [2022, submitted] for full details). Panels (C) illustrate electron temperature profiles of three shock crossing events. The x-axes show the profile along the shock normal, which means that the upstream is at higher values regardless of which direction the spacecraft crossed the shock. The shortest distance where half the temperature increase takes place is marked in grey.

shows that the temperature decrease from downstream to upstream takes place in two distinct steps with a plateau between them, similar to previous observations [Schwartz et al., 2011]. This is interpreted to be due to a very low ramp speed during the shock crossings. However, to investigate the electron heating scales, and to explain this profile, we need to estimate the speed of the shock ramp. To do this, we perform a four-spacecraft timing analysis on the temperature moments to obtain the shock ramp speed. This ramp speed estimate is shown in panel (Bf) and varies significantly across the interval of the shock. Considering the apparent changes in the ramp speed, to better reconstruct the true ramp profile, we instead use a modified version of the Spatio-Temporal Difference method developed by Shi et al. [2006] based on previous work on the dimensionality of plasma structures

[Shi et al., 2005]. The panels (C) shows the spatial profile of Te for the three events. The main results are

1. The ramp speed is highly variable within an individual shock crossing.

2. Large variation of the ramp speed and plateau of the temperature profile during the short crossing is possibly due to shock rippling or wave steepening.

3. At least half of the electron temperature increase takes place on ion scales.

4. Electron distributions in the ramp and downstream poorly match the Louville-mapped solar wind distribution and do not exhibit the typical flat-top distribution. This investigation also suggests that the electron heating across the shock is highly non-adiabatic.

3.2 Whistler waves and magnetic structures at the Venus bow shock

Although Venus is of comparable size and composition to Earth, decades of observations have confirmed that Venus lacks any significant intrinsic magnetic field. This presents some similarities to Earth (e.g., bow shock, magnetosheath, magnetotail), albeit with some fundamental differences such as a decreased bow shock stand-off distance (1-2 R_V), which is significantly closer than Earth (12 R_E), considering that $R_E \sim R_V \sim 6500$ km. The Solar Orbiter (SolO) mission is expected to perform several Venus gravity assist manoeuvres (VGAMs); the first (VGAM1) of these occurred on 27 December 2020, which was the focus of this study Dimmock et al. [2022].

Plotted in Figure 2 is a bow shock crossing by Solar Orbiter during a flyby. Panel (a) depicts the magnetic field in VSO coordinates, whereas panels (b-d) display the SCM magnetic field band-pass filtered between 30 and 120 Hz, electric field, and electron density, respectively. Since E_x was not measured, we define $E_\parallel$ and $E_\perp$ in panel (c) as the components of E along and perpendicular to the magnetic field in the YZ plane. Wavelet spectrograms of the AC electric field (e) and the magnetic field from the SCM (f) are also included. The remaining panels (f-j) provide a more detailed characterization of the fluctuations in terms of the degree of polarization (DOP), planarity, ellipticity, angle between the wave normal vector direction and the local magnetic field (θ_{kb}), and the Poynting flux. The solid line in panels (e-k) marks the lower hybrid frequency.

In both magnetic field and density, the shock transition exhibits highly non-laminar behaviour by the manifestation of complex multiscale structures across varying amplitudes. In addition, throughout the shock, some waves are right-handed and circularly polarised (ellipticity ~ 1) and the degree of polarization remains close to unity. Based on the right-hand polarization throughout the interval and frequencies below the local electron cyclotron frequency, we identify these waves as whistler-mode waves. Between 12:39:55.5-57, the wave vector normal direction is rather oblique to the background magnetic field and $\theta_{kb} \sim 45°$. In contrast, before 12:39:54.5, θ_{kb} is significantly more field-aligned and is $< 10°$. Therefore, changes in the wave properties across the shock are observed. It is also worth noting that the oblique waves appear somewhat separated from their

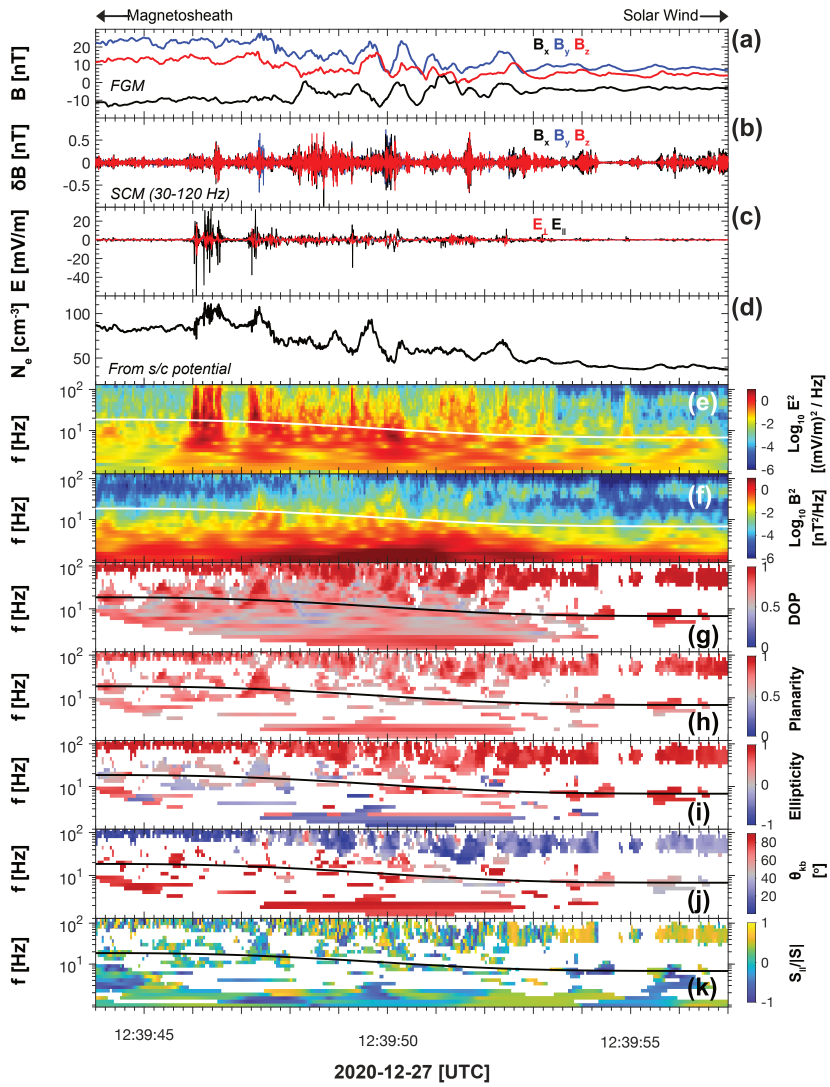

Figure 2: Polarization analysis of the magnetic and electric field across the shock front. Displayed in panels (a-d) are FGM magnetic field, SCM magnetic field (30-12 Hz), electric field, and electron density, respectively. Panels (e & f) are spectrograms of the electric field and SCM data. The remaining panels (g & h) correspond to the degree of polarization, planarity, ellipticity, θ_{kb}, and Poynting flux.

field-aligned counterparts as mentioned above. This is evident in the time series data plotted in panel (b) and the spectrogram in panel (f) by the clear isolated spectral power around 30 Hz after 12:39:55.5. There are also differences in the Poynting flux plotted in panel (j), which indicates that the directional energy flux is along the magnetic field direction ($S_{\|}/|S| \sim 1$), whereas this is substantially more disturbed deeper moving into the shock front, possibly indicating a source region for these waves.

The results from this study can be summarised by:

1. Solar Orbiter observed a highly structured Venusian bow shock with multiple large amplitude magnetic and density structures comparable to the shock amplitude in concert with higher frequency waves.

2. The shock substructures show many similarities to large amplitude whistler waves, which can be emitted by the shock ramp or be generated from instabilities.

3. Another explanation for shock front substructures is spatial variations on the shock surface known as ripples and this will become more apparent in forthcoming studies when the statistical characteristics of ripples are soundly established.

4. The shock substructures occur in concert with higher frequency whistler waves over the shock front between 30-120 Hz.

5. There is no clear temporal association between the lower frequency substructures and higher frequency whistler waves.

6. Higher frequency whistler waves show fascinating evolution across the shock front in terms of frequency and angle to the background magnetic field. This may indicate varying generation mechanisms within the shock (e.g., electron beams and temperature anisotropy) or interference from complex magnetic structures and electrostatic turbulence.

3.3 Whistler waves in the foot of the Earth bow shock

Many open questions remain on the topic of energy dissipation at collisionless shocks. Whistler waves are commonly observed near the shock front and are known to play an integral part in the dynamics and evolution of the shock itself. Their spatial and temporal scale allows them to mediate energy between ions and electrons, paving the way for the thermalization of cold solar wind plasma as it passes the shock. We analyzed whistler waves upstream of 11 supercritical and quasi-perpendicular shocks with MA ranging between 3.5 and 9.8, the fast mode Mach number, Mf, between 1.7 and 5.4, and θ_{Bn} between 55° and 82° (see Lalti et al. [2022]). Figure 3A shows an example of one event that was analysed in detail. Figure 3Aa-i shows the time series whereas 3B corresponds to ion VDFs at the time of the waves for three events. This event is shown in panels (Ba & Bd). The waves are clear in panels (A a-i) from the wavelet spectrogram and right-handed circularly polarised feature in panels (Af-i), respectively.

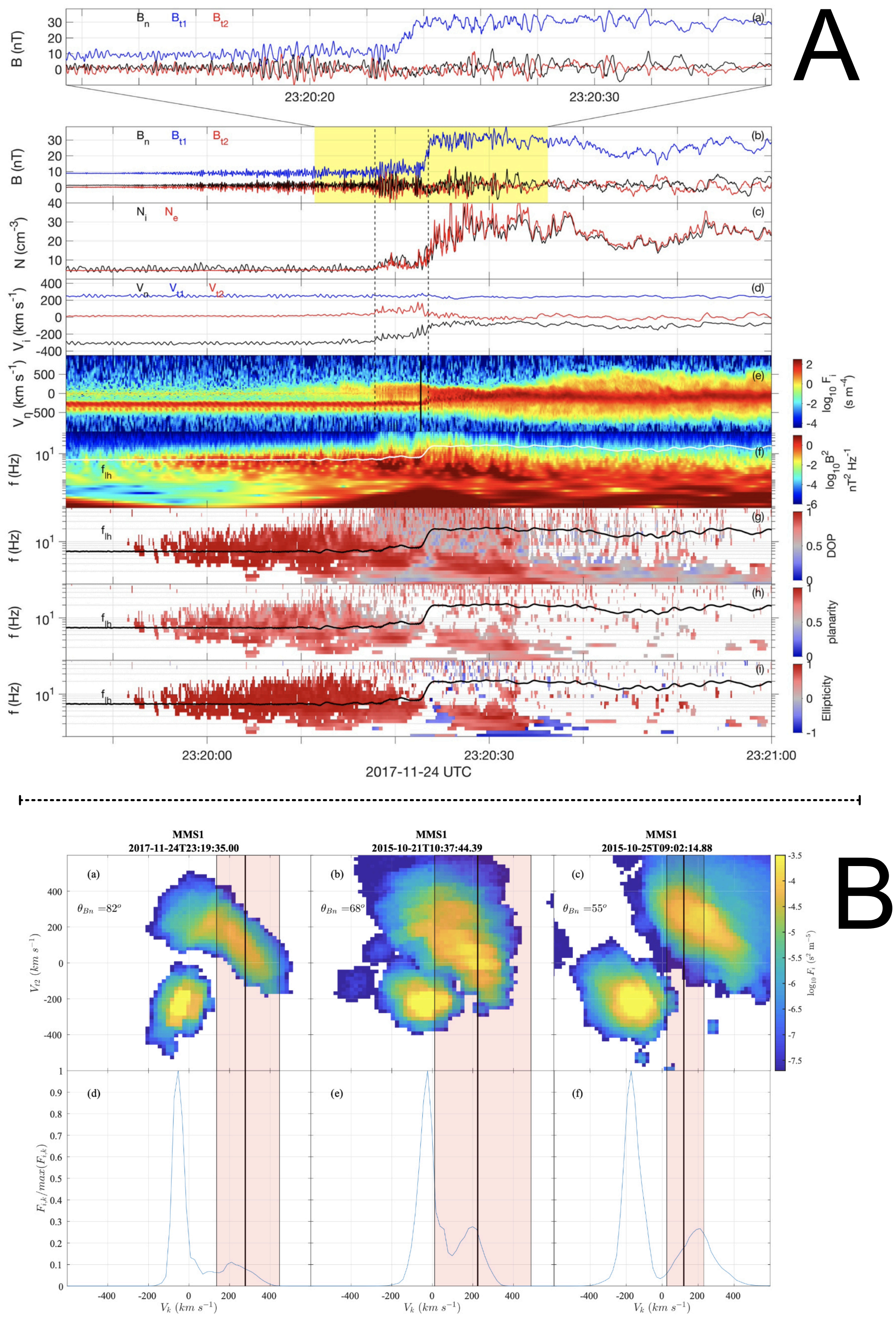

Figure 3: Panels (Aa-i): A shock crossing by MMS on 2017-11-24, 23:20 UT and wave polarization analysis. (a) Magnetic field enlarged around the foot and the ramp, (b) magnetic field, (c) electron and ion densities, (d) ion velocity, (e) 1D velocity distribution function reduced in the shock normal direction, (f) power spectrum of the magnetic field, (g) degree of polarization, (h) planarity, and (i) ellipticity. Panels (B): 2D Ion VDFs (top row) and 1D velocity distribution functions (VDFs) reduced in the **k** direction (bottom row) for three different events.

Shown in Figure 3B are the 2D ion VDFs for three events with different shock geometry, which included the event shown in panels A. The VDFs are plotted in the electron rest frame. One can see from the 2D VDFs that the reflected beam is in resonance with the waves and the part of the VDF. The resonance condition is satisfied for all 11 events analyzed in the study, suggesting that reflected ions generate the observed waves.

The main findings from this work were:

1. The wavelengths of these waves range from 0.7 to 1.7 ion inertial length and the wave-normal angle range from 20° to 42° with a k directed upstream of the shock and close to the shock coplanarity plane. The frequency of the waves in the solar wind frame ranges between 0.3 fLH and 1.2 fLH.

2. The highest wave amplitude is found in the foot, where we found the shock-reflected ion component in the distribution function. After reducing the observed 3D ion VDF in the direction of k, we find that the reflected ion component of the VDF is in Landau resonance with the observed waves, which indicates that the reflected ion beam is interacting with the observed whistlers and could be behind the generation of those waves.

3. Using a linear kinetic dispersion solver, we find that a VDF composed of a reflected ion beam on top of the incoming solar wind, with parameters taken from the observation, is unstable to the generation of whistler waves with properties close to what we observe. This supports the kinetic cross-field streaming instability between the reflected ions beam and the incoming solar wind electrons as a likely generation mechanism.

3.4 Shock Rippling

An important form of shock variability is shock rippling. For quasi-perpendicular shocks, this is a wave-like structure that propagates along the shock surface (tangential to the shock normal). In spacecraft measurements, this can manifest as changes in the magnetic field, density, and variations of the ion distributions. Figure 4A shows a rippled quasi-perpendicular shock from Johlander et al. [2022, submitted] whereas panels (B) show a rippled shock on 2016-01-06 UT.

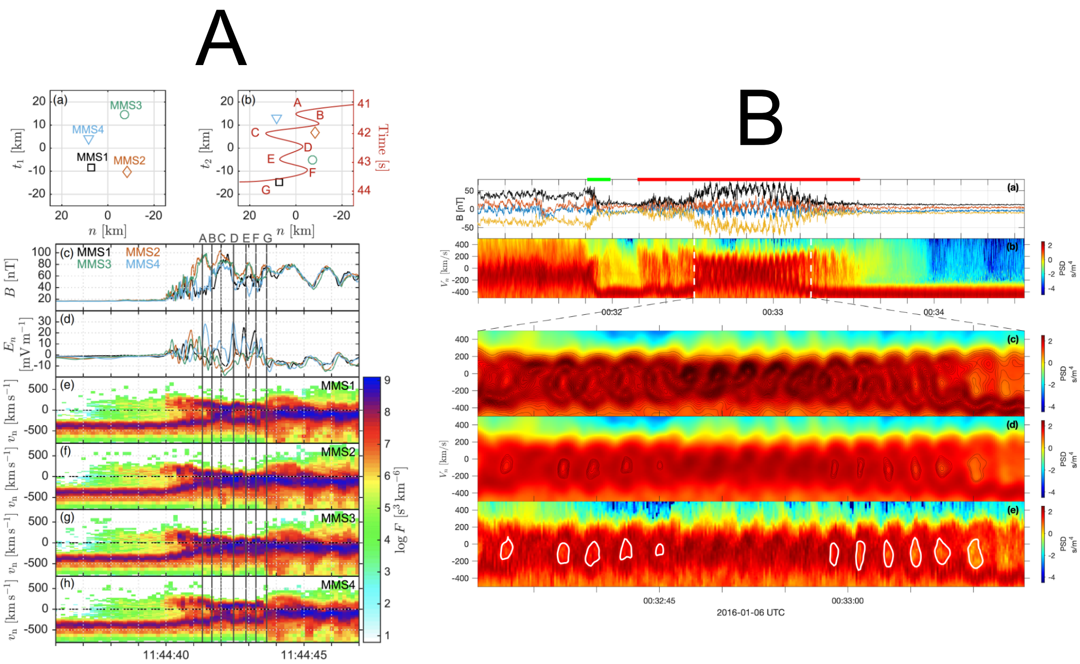

Figure 4: Panels (A) are taken from Johlander et al. [2016] and show a schematic (A a-b) of shock rippled and a rippled quasi-perpendicular shock observed by MMS (A c-h). Panels (B) also show a rippled quasi-perpendicular shock (B a-b). The remaining panels (B c-e) show the automatically identified phase-space holes by marking their borders with white lines.

Previous studies (e.g. Johlander et al. [2016]) and the work in this project have studied the behaviour of the shock during signatures of rippling. Yet, this has focused primarily on case studies and analysis of limited events. Rippled shocks appear to exhibit phase-space holes, as shown in panels (B c-e). We have developed a method to identify this feature to create a database of shocks with this behaviour. This is seen by the white boundaries plotted in panel (Bd). These shocks can be analyzed on a statistical basis to further our understanding of shock dynamics during this shock regime. This will be described in detail in the deliverable D3.2.

4 Conclusions

In this report, we have presented studies of shock variability, which in this context refers to temporal and spatial variations in the shock front. Examples of these are waves and instabilities, shock ripples, nonstationarity, reformation, and the motion of the shock itself. These studies reaffirm that the shock front, at different Mach numbers and on different planets is a complex combination of nonlinear structures that originate from different physical mechanisms. Furthermore, it is essential to separate these structures and identify the underlying physics to properly understand energy dissipation at the shock front. The main results from these studies are the following:

1. From studying the electron temperature across quasi-perpendicular shocks [Johlander et al., 2022, submitted], evidence suggests that changes in shock ramp speed and nonstationarity play a significant role in the electron temperature profile. The profile can also be highly non-adiabatic and almost half of the heating takes place on ion scales.

2. In this paper [Dimmock et al., 2022] we showed that whistler waves and nonstationary features are not mutually exclusive. Higher frequency whistler waves were likely driven by temperature anisotropies in the shock. Larger amplitude shock substructures show many similarities to large amplitude whistler waves, which can be emitted by the shock ramp or be generated from instabilities.

3. For whistler waves that were studied [Lalti et al., 2022], the highest wave amplitude is found in the foot, where we found the shock-reflected ion component in the distribution function. We propose the kinetic cross-field streaming instability (between the reflected ions beam and the incoming solar wind electrons) as a likely generation mechanism.

4. A signature of shock ripples is ion phase-space-holes [Johlander et al., 2016]. An automated method to identify these features was developed and will be used to study the behaviour of ion distributions during rippled quasi-perpendicular shocks.

5 References

A. P. Dimmock, Yu. V. Khotyaintsev, A. Lalti, E. Yordanova, N. J. T. Edberg, K. Steinvall, D. B. Graham, L. Z. Hadid, R. C. Allen, A. Vaivads, M. Maksimovic, S. D. Bale, T. Chust, V. Krasnoselskikh, M. Kretzschmar, E. Lorfèvre, D. Plettemeier, J. Souček, M. Steller, Š. Štverák, P. Trávníček, A. Vecchio, T. S. Horbury, H. O'Brien, V. Evans, and V. Angelini. Analysis of multiscale structures at the quasi-perpendicular Venus bow shock. Results from Solar Orbiter's first Venus flyby. *Astronomy & Astrophysics*, 660:A64, April 2022. doi: 10.1051/0004-6361/202140954.

A. Johlander, S. J. Schwartz, A. Vaivads, Yu. V. Khotyaintsev, I. Gingell, I. B. Peng, S. Markidis, P.-A. Lindqvist, R. E. Ergun, G. T. Marklund, F. Plaschke, W. Magnes, R. J. Strangeway, C. T. Russell, H. Wei, R. B. Torbert, W. R. Paterson, D. J. Gershman, J. C. Dorelli, L. A. Avanov, B. Lavraud, Y. Saito, B. L. Giles, C. J. Pollock, and J. L. Burch. Rippled quasiperpendicular shock observed by the magnetospheric multiscale spacecraft. *Phys. Rev. Lett.*, 117: 165101, Oct 2016. doi: 10.1103/PhysRevLett.117.165101.

A. Johlander, Yu. V. Khotyaintsev, A. P. Dimmock, D. B. Graham, and A Lalti. Rippled quasiperpendicular shock observed by the magnetospheric multiscale spacecraft. *Geophysical Research Letters*, 2022, submitted.

Ahmad Lalti, Yuri V. Khotyaintsev, Daniel B. Graham, Andris Vaivads, Konrad Steinvall, and Christopher T. Russell. Whistler waves in the foot of quasi-perpendicular supercritical shocks. *Journal of Geophysical Research: Space Physics*, 127(5):e2021JA029969, 2022. doi: https://doi.org/10.1029/2021JA029969. e2021JA029969 2021JA029969.

Steven J. Schwartz, Edmund Henley, Jeremy Mitchell, and Vladimir Krasnoselskikh. Electron temperature gradient scale at collisionless shocks. *Phys. Rev. Lett.*, 107:215002, Nov 2011. doi: 10.1103/PhysRevLett.107.215002.

Q. Q. Shi, C. Shen, Z. Y. Pu, M. W. Dunlop, Q.-G. Zong, H. Zhang, C. J. Xiao, Z. X. Liu, and A. Balogh. Dimensional analysis of observed structures using multipoint magnetic field measurements: Application to cluster. *Geophysical Research Letters*, 32(12), 2005. doi: https://doi.org/10.1029/2005GL022454.

Q. Q. Shi, C. Shen, M. W. Dunlop, Z. Y. Pu, Q.-G. Zong, Z. X. Liu, E. Lucek, and A. Balogh. Motion of observed structures calculated from multi-point magnetic field measurements: Application to cluster. *Geophysical Research Letters*, 33 (8), 2006. doi: https://doi.org/10.1029/2005GL025073.

A Appendix

Attached is the pre-print for the manuscript Johlander et al. [2022, submitted].

Electron heating scales in collisionless shocks measured by MMS

Andreas Johlander[1], Yuri V. Khotyaintsev[1], Andrew P. Dimmock[1], Daniel B. Graham[1], Ahmad Lalti[1,2]

[1]Swedish Institute of Space Physics, Uppsala, Sweden
[2]Space and Plasma Physics, Department of Physics and Astronomy, Uppsala University, Uppsala, Sweden

Key Points:

- Using multipoint data from MMS, we find that electron heating takes place on ion scales in the quasi-perpendicular shock ramp
- We show that the time series of the temperature does not represent the spatial profile due to varying shock ramp speed
- Electron distributions in the ramp and downstream of the shock show that electrons are heated non-adiabatically

Abstract
Electron heating at collisionless shocks in space is a combination of adiabatic heating due to large-scale electric and magnetic fields and non-adiabatic scattering by high-frequency fluctuations. The scales at which heating happens can hint to what physical processes are taking place. In this letter, we study electron heating scales with data from the Magnetospheric Multiscale (MMS) spacecraft at Earth's quasi-perpendicular bow shock. We utilize the tight tetrahedron formation and fast plasma measurements of MMS to directly measure the electron temperature gradient. From this, we reconstruct the electron temperature profile inside the shock ramp and find that the electron temperature increase takes place on ion scales. Further, we use Liouville mapping to investigate the high-cadence electron distributions through the ramp to estimate the deHoffmann-Teller potential and electric field. We find that electron heating is highly non-adiabatic at the high-Mach number shocks studied here.

Plain Language Summary

Shock waves appear whenever a supersonic medium, such as a plasma, encounters an obstacle. The plasma, which consists of charged ions and free electrons, is heated by the shock wave through interactions with the electromagnetic fields. In this work, we investigate how electrons are heated at plasma shocks. A key parameter to electron heating is the thickness of the layer where the heating takes place. Here, we use observations from the four Magnetospheric Multiscale spacecraft that regularly cross the standing bow shock that forms when the supersonic plasma, known as the solar wind, encounters Earth's magnetic field. We find that the thickness of the shock is larger than previously reported and is on the scales where ion physics dominate. We also find that the electron heating deviates significantly from simple adiabatic heating.

Introduction

Shock waves appear in a wide variety in space plasmas where they act to slow down and heat supersonic flows before the plasma can encounter an obstacle. Plasma shocks in the heliosphere and in astrophysical settings are often collisionless, meaning that heating and entropy generation takes place through interactions between the particles and the electromagnetic fields [Krall, 1997, Parks et al., 2017]. Due to the collisionless nature of the shock waves, energy is not partitioned equally between the plasma species. Ions, which gain most of the dissipated energy [e.g., Schwartz et al., 1988, Vink et al., 2015], are principally heated by the instability between gyrobunched shock-reflected and the transmitted ions [Sckopke et al., 1983].

Electron heating happens in an interplay between the betatron effect through an increase in magnetic field and the electric cross-shock potential (DC fields) on one hand and wave-particle interactions (AC fields) at the shock [Goodrich & Scudder, 1984, Scudder, 1995]. Since electron thermal speeds in the solar wind are much greater than the bulk speed, electrons are free to move across the shock along the magnetic field in both directions. The DC fields act to adiabatically inflate the distribution in velocity space, leaving a hole in velocity space. This phase-space inflation is reversible and does therefore not produce entropy [Balikhin et al., 1993, Lindberg et al., 2022]. The hole left in velocity is filled by electron scattering by AC fields, which leads to a flat-top electron distribution downstream of the shock [Feldman et al., 1983]. Through which processes the non-reversible heating takes place in shocks is not fully understood but short-wavelength electrostatic waves, which likely form from the instability from the inflation of the electron distributions, have been observed at the shock with amplitudes which suggests that they can efficiently scatter electrons [e.g., Bale et al., 1998, Vasko et al., 2018, Vasko et al., 2022].

An insight into the electron heating process in the shock can be achieved by measuring the width of the ramp. With multi-spacecraft missions, this is a seemingly straightforward measurement which has been performed several times. Newbury et al. [1998] used observations by the two ISSE spacecraft and found ramp widths around or below the ion inertial scale and noted the presence of smaller scale structures within the ramp. Bale et al. [2003] on the other hand reported that ramp thickness scales with the gyroradius of shock-reflected ions. Hobara et al. [2010] used observations of the bow shock by the Cluster and Themis spacecraft and found that the ramp width is of the order of the ion inertial length and decreases with Mach number. The most detailed investigation of the heating scales to date was done by Schwartz et al. [2011] who used a slow shock crossing observed by Cluster to measure the ramp width using direct measurements of the electron temperature. The authors found that half of the total temperature increase took place on only a few electron inertial lengths, significantly smaller than previously reported.

In this work, we revisit the topic of electron heating scales at collisionless shocks using observations from the Magnetosperic Multiscale (MMS) spacecraft. With the high time-resolution electron observations, in combination with the tight tetrahedron formation of MMS, we perform the most accurate and detailed measurement of the electron temperature gradient in the ramps of three quasi-perpendicular shocks. We further estimate the deHoffmann-Teller potential and reconstruct the electric field in this frame inside the shock ramp and use this to characterize the contributions to electron heating at shocks.

Observations

We use observations by the four MMS spacecraft [Burch et al., 2016]. Magnetic field data are from the fluxgate magnetometer [Russell et al., 2016] which provides data with a cadence of 128 Hz. Particle data are from the Fast Plasma Investigation (FPI) instrument which measures the electron and ion distributions and moments every 30 ms and 150 ms respectively [Pollock et al., 2016]. Since FPI is not designed for the cold and fast solar wind, we obtain the proton temperature used to calculate the magnetosonic Mach numbers from Solar Wind Experiment onboard the upstream Wind spacecraft [Ogilvie et al., 1995], time-shifted and obtained from the OMNI database [King & Papitashvili, 2005]. We also validate the upstream electron temperature from MMS with Wind measurements using the time-lag given by OMNI, see Table 1.

We select three quasi-perpendicular bow shock crossings from the MMS data from 2015 to 2018 when electron data from FPI onboard all four spacecraft is available. In the selection, we used the following criteria to find suitable events: (a) the shock crossing should be fast, so that time-evolution of the ramp plays a limited role, (b) all four spacecraft should be in the ramp at the same time, and (c) the four-spacecraft measurements in electron temperature should be clearly separated so that the gradient of electron temperature can be measured accurately. This selection resulted in three shock crossings from hundreds of available quasi-perpendicular shock crossings available from this time [Lalti et al., 2022] meaning that these criteria are rarely satisfied by MMS at the bow shock due to the typically very small spacecraft separation. This is an early indication that the temperature gradient scales at the shock are larger than the typical MMS separation of $5-30$ km.

An overview of one of the elected events, named Event 1, observed by MMS1 is shown in Figure 1. The spacecraft crosses the bow shock from the downstream magnetosheath and into the upstream solar wind. The shock ramp is seen as a sharp boundary in number density N and electron temperatures. The parallel and perpendicular temperatures are similar in the ramp and downstream of the shock with temperature anisotropy close to 1. We therefore from now on consider the scalar electron temperature $T_e{=}(2T_{e,\perp}{+}T_{e,\|})/3$. We determine the shock normal of this shock and the other two events by selecting up-and downstream time intervals and using the mixed mode method [Abraham-Shrauner, 1972, Schwartz, 1998]. We find that the shock shown in Figure 1 is quasi-perpendicular with $\theta_{\rm Bn}$=73° and moderately-high Mach number with M_A=9. These and other shock parameters for all events are listed in Table 1. The three selected events are quasi-perpendicular and have relatively high Alfvén Mach numbers.

Electron heating scales

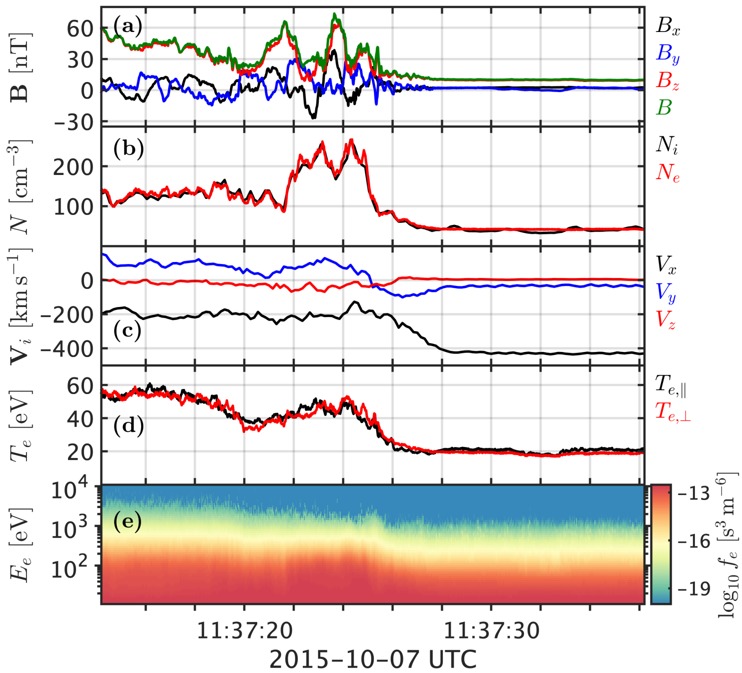

Figure 1. Shock crossing by MMS1. (a) Magnetic field **B** in GSE coordinates. (b) Ion and electron number densities $N_{i,e}$. Ion flow velocity $\mathbf{V}_i$. (e) omni-directional electron phase-space density as a function of energy.

To investigate the electron heating scales we now look at the four-spacecraft observations from the shock crossing, shown in Figure 2. Panel (c) shows the four-spacecraft observations of T_e for Event 1. We can see that the temperature decrease from downstream to upstream takes place in two distinct steps with a plateau between them, similar to previous observations [Schwartz et al., 2011]. It is possible to perform a four-spacecraft timing analysis to obtain the shock ramp speed from the temperature measurements. However, this would be sensitive to what parts of the ramp are being used to find the time-shifts, which may indicate that the shock ramp speed is varying even during this fast shock crossing. The change in ramp speed could possibly be related to shock rippling [e.g., Winske & Quest, 1988, Johlander et al., 2016], wave steepening [e.g., Krasnoselskikh et al., 2002, Dimmock et al., 2019], or, perhaps less likely due to the short crossing time, changes in the overall shock speed due to varying upstream conditions [Maksimovic et al., 2003].

Considering the apparent changes in the ramp speed, to better reconstruct the true ramp profile, we instead use a modified version of the Spatio-Temporal Difference method developed by Shi et al. [2006] based on previous work on dimensionality of plasma structures [Shi et al., 2005]. The original method uses multi-point measurements of the magnetic field vector. With FPI's high cadence plasma measurements onboard MMS, it is possible to extend this method to plasma quantities such as T_e. Using this quantity, we can, like Schwartz et al. [2011], directly measure the electron heating scales without relying on proxies such as magnetic field or density. The spatio-temporal difference method uses the material derivative of the plasma with the assumption of quasi-stationarity, i.e., that local changes are small compared to the convection of the shock [Shi et al., 2006]. This means that

$$\frac{\mathrm{d}T_e}{\mathrm{d}t} = -\mathbf{V}_\mathrm{r} \cdot \nabla T_e, \tag{1}$$

where $\mathrm{d}T_e/\mathrm{d}t$ is the time derivative of the time series of T_e observed by the spacecraft, ∇T_e is the temperature gradient obtained through multi-point measurements [Chanteur, 1998], and $\mathbf{V}_\mathrm{r}$ is the instantaneous ramp velocity in the spacecraft frame of reference. Unlike in the analysis by Shi et al. [2006], since we use a scalar quantity for the method, it is only possible to obtain the maximum derivative direction which simply takes the form $\hat{\mathbf{n}}_1 = \nabla T_e/|\nabla T_e|$ and $\mathbf{V}_\mathrm{r} = V_\mathrm{r}\hat{\mathbf{n}}_1$. We then obtain the ramp speed

$$V_\mathrm{r} = -\frac{\Delta\langle T_e\rangle}{\Delta t|\nabla T_e|}, \tag{2}$$

where $\Delta\langle T_e\rangle$ is the change of the four-spacecraft average of T_e and Δt is the time step between measurements.

The method to obtain the ramp speed is illustrated in Figure 2. The spacecraft were at the time of the crossing in a tetrahedron formation with average inter-spacecraft distance of 27 km. Figure 2d shows the terms used in equation (2). To avoid the influence of small-scale fluctuations and noise in T_e and at the same time fulfill $\langle r_{\alpha\beta}\rangle \gg V_\mathrm{r}\Delta t$ [Shi et al., 2006], the electron data here are downsampled to 150 ms resolution. The time interval used to obtain the ramp speed is marked in gray. The resulting unit vector $\hat{\mathbf{n}}_1$ is rotated into a Cartesian coordinate system aligned with the shock and the magnetic field, where $\hat{\mathbf{n}}$ is the shock normal, $\hat{\mathbf{t}}_1$ lies in the coplanarity plane, and $\hat{\mathbf{t}}_2$ is out-of-plane, see [e.g., Johlander et al., 2018]. We see in panel (e) that ∇T_e and $\hat{\mathbf{n}}_1$ are essentially anti-parallel to $\hat{\mathbf{n}}$ throughout the ramp interval and deviates at most 30° from this direction. The resulting ramp speed along $\hat{\mathbf{n}}_1$ is shown in Figure 2f and, supporting our initial suspicion, does vary during the crossing. The ramp speed starts out at $\sim$50 km s^{-1} and goes to zero and then back up, corresponding to the two jumps and the plateau in T_e profile. The mean ramp speed along $\hat{\mathbf{n}}$ in this case is -45 km s^{-1} which is slightly lower than the speed obtained from four-spacecraft timing of -59 ± 7 km s^{-1} [Vogt et al., 2011].

The next step is to obtain the electron heating scale of the shock. To obtain the shock ramp temperature profile, we integrate $\mathbf{V}_\mathrm{r}$ over time to obtain the spacecraft position $\mathbf{s}$ relative to the shock. The temperature profiles along $\hat{\mathbf{n}}$ for Event 1 are shown in Figure 3a. We can see that the temperature change takes place over nearly 100 km, which is larger than the upstream ion inertial length and significantly larger than reported by Schwartz et al. [2011]. We can also see that that the plateau seen in T_e in the time series in Figure 2c is not present in the spatial profile due to the decrease in $\mathbf{V}_r$ in the middle of the ramp. This highlights the fact that spacecraft time series observations do not always correspond to spatial profiles at nonstationary or evolving shocks.

We repeat the calculations above for the other two events. Figure 3 shows the spatial profile of T_e for the three events. Figures showing the calculation of $\mathbf{V}_r$ for these events can be found in Figures S1 and S2 in the Supporting Information. Events 2 and 3 show similar spatial profiles with heating scales comparable to the upstream ion inertial length $d_{i,u}$. We define the *electron heating scale* as the shortest distance where half the temperature increase between $T_{e,u}$ and the maximum T_e in the selected ramp interval. These distances are shaded with gray in Figure 3 and the scales are listed in Table 1. We see that for these three events, the electron heating scales are $\sim 0.5-1 d_{i,u}$, which is similar to that found by Hobara et al. [2010], but significantly larger than the results by Schwartz

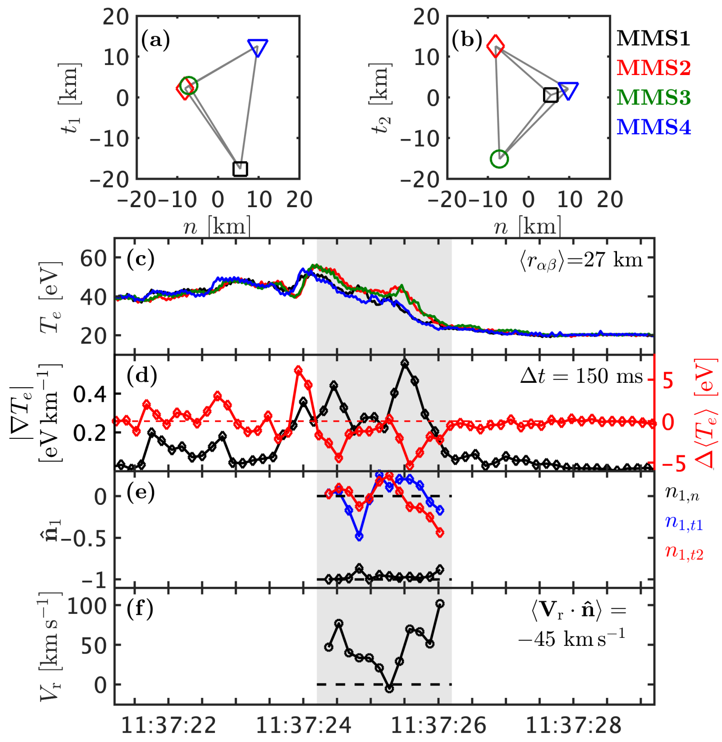

Figure 2. Shock crossing seen by the four spacecraft. (a-b) relative spacecraft positions in the $n{-}t_1$ and $n{-}t_2$ planes. (c) four-spacecraft measurements of T_e. (d) left: $|\nabla T_e|$ in black and right: $\Delta\langle T_e\rangle$ in red. (e) maximum derivative direction $\hat{\mathbf{n}}_1$ (f) V_r calculated from eq. (2).

et al. [2011]. These electron heating scales are also significantly smaller than the density gradient scales reported by Bale et al. [2003].

Table 1. Shock and upstream parameters for the events studied.

Parameter	Event 1	Event 2	Event 3
Date	2015-10-07	2015-12-28	2018-03-17
Time (UTC)	11:37	05:29	22:21
θ_{Bn} [°]	73	51	89
Alfvén Mach number M_A	9	17	10
Fast mode Mach M_f	4	9	6
Electron temp. $T_{e,u}$ [eV]	20	8	11
$T_{e,u}$ measured by Wind [eV]	18	9	12
Max T_e in ramp [eV]	51	56	48
Electron beta $\beta_{e,u}$	2.9	1.9	1.2
Avg. s/c separation $\langle r_{\alpha\beta}\rangle$ [km]	27	34	25
Ion inertial length $d_{i,u}$ [km]	37	88	90
Electron heating scale [km]	42	69	57

We conclude this section with a short discussion on the results. Here, we select three shock crossings by MMS. In the selection, we have gone through hundreds of shocks crossings in search for suitable candidates. The inter-spacecraft separation of MMS during the time we investigated is normally 5−30 km at the bow shock, which means that we clearly have a selection bias toward large spacecraft separations, see Table 1. In fact, when the spacecraft are closer together, the measurements of T_e are too close to accurately determine ∇T_e, which means that it is essentially a single-point measurement. This selection bias in our events could indicate that the heating scales that we obtain should be considered as a lower limit.

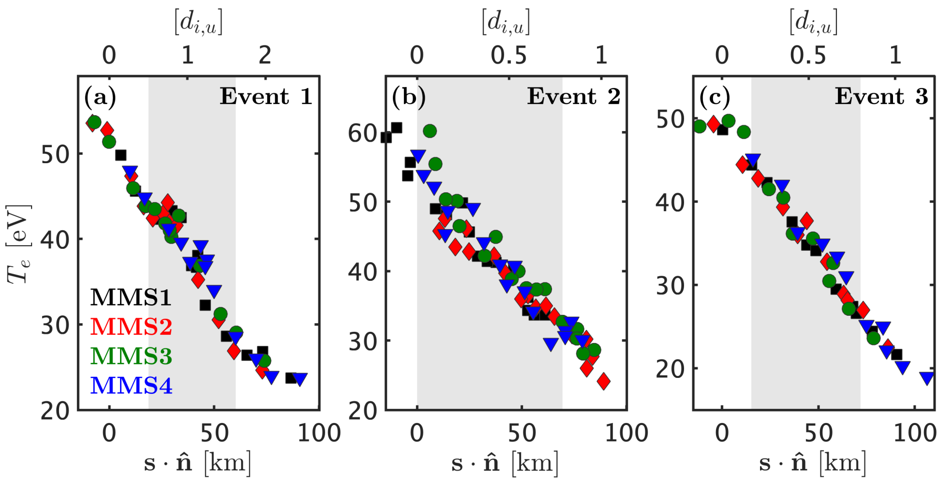

Figure 3. Electron temperature profiles for the three shock crossing events. The x-axes show the profile along $\hat{\mathbf{n}}$ which means that upstream is at higher values regardless of which direction the spacecraft crossed the shock. Units are km on the bottom and $d_{i,u}$ on the top. The shortest distance where half the temperature increase takes place is marked in gray.

Cross-shock potential

We have found that electron heating takes place on ion scales at quasi-perpendicular shocks. Next, we investigate how the electrons are heated. Due to the relatively large heating scales, one could possibly expect that the magnetic moment of the electrons be conserved, at least in the absence of wave-particle interactions [Balikhin et al., 1993]. To compare the observed electron distributions to those produced by adiabatic heating, we need to measure the cross-shock potential in the deHoffmann-Teller frame [de Hoffmann & Teller, 1950] ϕ^{HT}. The most reliable way to do this [Schwartz et al., 2021] is to perform a Liouville mapping of the electron distribution.

We start by reordering the electron distribution in the spacecraft rest frame to a Cartesian field-aligned velocity grid $(v_\parallel, v_\perp)$ by interpolating and averaging the 3D measured distribution. We select a time interval in the solar wind and use the average distribution as a reference distribution f_{ref}. We then obtain the Lioville-mapped distribution $f_{\mathcal{L}}$ using the measured B and a guess of ϕ^{HT} using the method described by Lefebvre et al. [2007]. This mapping assumes conservation of the magnetic moment and therefore adiabatic electron heating. The mapping is done by assuming gyrotropic distributions and tracing electron trajectories to or from the reference distribution and assuming constant phase-space density along the trajectories. Since we are mainly interested in ϕ^{HT} in the shock ramp, we ignore the effects from the overshoot. Also, unlike Lefebvre et al. [2007], we find the ϕ^{HT} by minimizing a quantity with a similar definition to non-Maxwellianity [Graham et al., 2021] which adopts a value between 0 and 1 and in this coordinate system becomes

$$\epsilon_{\mathcal{L}} = \frac{2\pi}{n_e + n_{\mathcal{L}}} \int \left| f_e(v_\parallel, v_\perp) - f_{\mathcal{L}}(v_\parallel, v_\perp) \right| v_\perp \mathrm{d}v_\parallel \mathrm{d}v_\perp, \tag{3}$$

where f_e is the measured electron distribution and n_e and n_L are the measured and mapped number density respectively. For this case we limit the calculation of $\epsilon_{\mathcal{L}}$ to parts of velocity space where $f_e \in [5\times10^{-17}, 5\times10^{-15}]\ \mathrm{s^3\,m^{-6}}$, which is below the solar wind peak f_e and above the noise limit, where the assumption of adiabatic heating can be expected to be fulfilled.

Figure 4 shows the results from the Liouville mapping for Event 1. We see that ϕ^{HT} reaches values of $\sim$150 eV, similar to previously reported values at Earth's bow shock [e.g., Lefebvre et al., 2007, Schwartz et al., 2021]. Panels (d-f) show electron distributions in the marked times in the downstream, ramp, and solar wind. The regions of velocity space determined by the limits of f_e are shown by gray lines. The multi-point measurements of ϕ^{HT} inside the ramp offer a unique opportunity to directly measure the deHoffmann-Teller electric field in the shock, something that is not possible with electric field instruments [Schwartz et al., 2021]. Again, under the assumption of quasi-stationarity, this electric field is simply $\mathbf{E}^{\mathrm{HT}} = -\nabla\phi^{\mathrm{HT}}$. We see that $\mathbf{E}^{\mathrm{HT}}$ reconstructed from the cross-shock potential is mainly along $\hat{\mathbf{n}}$ as expected, and reaches a value of $\sim$2 $\mathrm{mV\,m^{-1}}$.

We now look closer at the electron distribution function inside of the shock ramp in Figure 4g-i. We see the distribution mapped from the solar wind to the ramp in red and the actual measured distribution in black. It is clear that the measured electron distribution is less steep than expected by mapping the solar wind electron distribution to the ramp. The same trend (not shown) persists throughout the downstream region and shows that electrons undergo strong non-adiabatic heating. The same trend is visible in the other two events studied here, which all have relatively high Mach numbers. However, we find electron distributions in much better agreement with adiabatic heating at low-Mach shocks, see Figure S3 in the Supporting Information. It is worth noting that the mismatch in slopes in Figure 4g-i is present in both the parallel and anti-parallel directions, which in this case corresponds to toward upstream and downstream respectively. This indicates that electrons crossing from upstream to downstream are accelerated by some process while electrons crossing in the opposite direction are simultaneously decelerated compared to simple adiabatic heating/cooling.

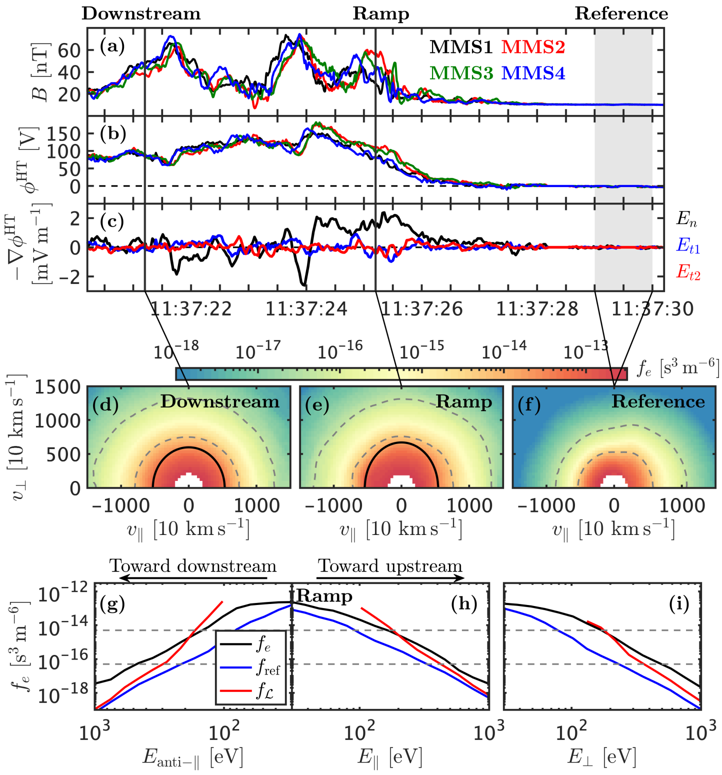

Figure 4. Results from Liouville mapping for the four MMS spacecraft. Time series of: (a) B, (b) ϕ^{HT}, (c) the deHoffmann-Teller frame electric field from $-\nabla\phi^{\mathrm{HT}}$. Times in the downstream, ramp, and interval for the reference distributions are marked. (d-f) corresponding electron distributions for the three times measured by MMS1. Mapping limits are shown by gray dashed lines. The solid black lines mark areas where no trajectory can be traced to or from the solar wind. (g-i) line plots showing electron distributions in the (anti-)parallel and perpendicular directions (10° bins) in the shock ramp. Black lines show the measured distribution in the ramp, blue lines are from the solar wind, and red lines are the mapped solar wind distributions.

Conclusions

We investigate the scales at which electrons are heated in quasi-perpendicular collisionless shocks. We use MMS observations from three separate encounters with Earth's bow shock and apply the spatio-temporal difference method [Shi et al., 2006] to obtain the spatial electron temperature profiles. This provides the to date most accurate and reliable estimate of the electron heating scales at shocks. We find that at least half the total temperature increase takes place on ion scales $\sim 0.5-1 d_{i,u}$, in line with some previous multi-spacecraft measurements [Hobara et al., 2010] but significantly larger than reported by Schwartz et al. [2011].

In one of the studied events, we find that the electron temperature rise from upstream to downstream takes place in two discreet steps with a plateau between them. Multi-spacecraft data reveals that there is still a significant temperature gradient during the plateau, which likely means that the ramp speed is close to zero. Such variation of the ramp speed during the short crossing is possibly due to shock rippling [Johlander et al., 2016] or wave steepening [Krasnoselskikh et al., 2002]. The actual spatial temperature profile is therefore more monotonic across the shock ramp than can be guessed from the time series of T_e. This highlights the often overlooked fact that time series data not necessarily correspond to spatial profiles at Earth's highly dynamical bow shock.

Last, we investigate how the electrons are heated through the shock ramp and into the downstream. We infer the deHoffmann-Teller cross-shock potential from Liouville mapping [Lefebvre et al., 2007] the high-cadence measured electron distribution functions. Thanks to the multi-point measurements, we can for the first time directly estimate the deHoffmann-Teller electric field inside of the shock ramp and find that its directed along the shock normal and reaches a value of $\sim$2 mV m^{-1}. Furthermore, we find that the electron distributions in the ramp and downstream poorly match the mapped solar wind distribution and do not exhibit the typical flat-top distribution. This means that the electron heating is highly non-adiabatic. We find indications that the electron distribution behave more adiabatically at lower Mach numbers, see Figure S3. Future work should focus on the parametric dependence on electron heating in the shock combined with identifying the processes responsible for scattering and non-reversible heating at the shock.

Data Availability Statement

The MMS data are available through the MMS Science Data Center `https://lasp.colorado.edu/mms/sdc/public/`. The OMNI data are available from the GSFC/SPDF OMNIWeb interface `https://omniweb.gsfc.nasa.gov`. The Wind data are available from `https://wind.nasa.gov/` Data analysis was performed using the IRFU-Matlab analysis package available at `https://github.com/irfu/irfu-matlab`

Acknowledgments

This research was made possible with the data and efforts of the people of the MMS mission. The work was funded by the SHARP project under the European Union's Horizon 2020 research and innovation program with grant agreement number 101004131. APD received financial support from the Swedish National Space Agency (SNSA) Grant 2020-00111, DBG from SNSA Grant 128/17, and AL from the Swedish Research Council Grant 2018-05514.

References

Abraham-Shrauner, B. (1972). Determination of magnetohydrodynamic shock normals. *J. Geophys. Res.*, *77*, 736. doi: 10.1029/JA077i004p00736

Bale, S. D., Kellogg, P. J., Larsen, D. E., Lin, R. P., Goetz, K., & Lepping, R. P. (1998, January). Bipolar electrostatic structures in the shock transition region: Evidence of electron phase space holes. *Geophys. Res. Lett.*, *25*(15), 2929-2932. doi: 10.1029/98GL02111

Bale, S. D., Mozer, F. S., & Horbury, T. S. (2003, December). Density-Transition Scale at Quasiperpendicular Collisionless Shocks. *Phys. Rev. Lett.*, *91*(26), 265004. doi: 10.1103/PhysRevLett.91.265004

Balikhin, M., Gedalin, M., & Petrukovich, A. (1993, Mar). New mechanism for electron heating in shocks. *Phys. Rev. Lett.*, *70*, 1259–1262. Retrieved from `https://link.aps.org/doi/10.1103/PhysRevLett.70.1259` doi: 10.1103/PhysRevLett.70.1259

Burch, J. L., Moore, T. E., Torbert, R. B., & Giles, B. L. (2016, March). Magnetospheric Multiscale Overview and Science Objectives. *Space Sci. Rev.*, *199*, 5-21.

doi: 10.1007/s11214-015-0164-9

Chanteur, G. (1998). Spatial Interpolation for Four Spacecraft: Theory. *ISSI Scientific Reports Series*, *1*, 349-370.

de Hoffmann, F., & Teller, E. (1950, Nov). Magneto-hydrodynamic shocks. *Phys. Rev.*, *80*, 692–703. Retrieved from `http://link.aps.org/doi/10.1103/PhysRev.80.692` doi: 10.1103/PhysRev.80.692

Dimmock, A. P., Russell, C. T., Sagdeev, R. Z., Krasnoselskikh, V., Walker, S. N., Carr, C., ... Balikhin, M. A. (2019, February). Direct evidence of nonstationary collisionless shocks in space plasmas. *Science Advances*, *5*(2), eaau9926. doi: 10.1126/sciadv.aau9926

Feldman, W. C., Anderson, R. C., Bame, S. J., Gary, S. P., Gosling, J. T., McComas, D. J., ... Hoppe, M. M. (1983, January). Electron velocity distributions near the earth's bow shock. *J. Geophys. Res.*, *88*(A1), 96-110. doi: 10.1029/JA088iA01p00096

Gedalin, M. (2021, May). Shock Heating of Directly Transmitted Ions. *Astrophys. J. Lett.*, *912*(2), 82. doi: 10.3847/1538-4357/abf1e2

Goodrich, C. C., & Scudder, J. D. (1984, August). The adiabatic energy change of plasma electrons and the frame dependence of the cross-shock potential at collisionless magnetosonic shock waves. *J. Geophys. Res. (Space Physics)*, *89*(A8), 6654-6662. doi: 10.1029/JA089iA08p06654

Graham, D. B., Khotyaintsev, Y. V., André, M., Vaivads, A., Chasapis, A., Matthaeus, W. H., ... Gershman, D. J. (2021). Non-maxwellianity of electron distributions near earth's magnetopause. *Journal of Geophysical Research: Space Physics*, *126*(10), e2021JA029260. Retrieved from `https://agupubs.onlinelibrary.wiley.com/doi/abs/10.1029/2021JA029260` (e2021JA029260 2021JA029260) doi: https://doi.org/10.1029/2021JA029260

Hobara, Y., Balikhin, M., Krasnoselskikh, V., Gedalin, M., & Yamagishi, H. (2010). Statistical study of the quasi-perpendicular shock ramp widths. *Journal of Geophysical Research: Space Physics*, *115*(A11). Retrieved from `https://agupubs.onlinelibrary.wiley.com/doi/abs/10.1029/2010JA015659` doi: https://doi.org/10.1029/2010JA015659

Johlander, A., Schwartz, S. J., Vaivads, A., Khotyaintsev, Y. V., Gingell, I., Peng, I. B., ... Burch, J. L. (2016, Oct). Rippled quasiperpendicular shock observed by the magnetospheric multiscale spacecraft. *Phys. Rev. Lett.*, *117*, 165101. Retrieved from `http://link.aps.org/doi/10.1103/PhysRevLett.117.165101` doi: 10.1103/PhysRevLett.117.165101

Johlander, A., Vaivads, A., Khotyaintsev, Y. V., Gingell, I., Schwartz, S. J., Giles, B. L., ... Russell, C. T. (2018). Shock ripples observed by the mms spacecraft: ion reflection and dispersive properties. *Plasma Physics and Controlled Fusion*, *60*(12), 125006. doi: 10.1088/1361-6587/aae920

King, J. H., & Papitashvili, N. E. (2005, February). Solar wind spatial scales in and comparisons of hourly Wind and ACE plasma and magnetic field data. *Journal of Geophysical Research (Space Physics)*, *110*, A02104. doi: 10.1029/2004JA010649

Krall, N. A. (1997, September). What do we really know about collisionless shocks? *Advances in Space Research*, *20*(4-5), 715-724. doi: 10.1016/S0273-1177(97)00461-4

Krasnoselskikh, V. V., Lembège, B., Savoini, P., & Lobzin, V. V. (2002, April). Nonstationarity of strong collisionless quasiperpendicular shocks: Theory and full particle numerical simulations. *Physics of Plasmas*, *9*, 1192-1209. doi: 10.1063/1.1457465

Lalti, A., Khotyaintsev, Y. V., Dimmock, A. P., Johlander, A., Graham, D. B., & Olshevsky, V. (2022). *A database of mms bow shock crossings compiled using machine learning.* arXiv. Retrieved from `https://arxiv.org/abs/2203.04680` doi: 10.48550/ARXIV.2203.04680

Lefebvre, B., Schwartz, S. J., Fazakerley, A. F., & Décréau, P. (2007, September). Electron dynamics and cross-shock potential at the quasi-perpendicular Earth's bow shock. *Journal of Geophysical Research (Space Physics)*, *112*(A9), A09212. doi: 10.1029/2007JA012277

Lindberg, M., Vaivads, A., Raptis, S., Lindqvist, P.-A., Giles, B. L., & Gershman, D. J. (2022). Electron kinetic entropy across quasi-perpendicular shocks. *Entropy*, *24*(6). Retrieved from `https://www.mdpi.com/1099-4300/24/6/745` doi: 10.3390/e24060745

Maksimovic, M., Bale, S. D., Horbury, T. S., & André, M. (2003, April). Bow shock motions observed with CLUSTER. *Geophys. Res. Lett.*, *30*, 46-1. doi: 10.1029/2002GL016761

Newbury, J. A., Russell, C. T., & Gedalin, M. (1998, December). The ramp widths of high-Mach-number, quasi-perpendicular collisionless shocks. *J. Geophys. Res.*, *103*(A12), 29581-29594. doi: 10.1029/1998JA900024

Ogilvie, K. W., Chornay, D. J., Fritzenreiter, R. J., Hunsaker, F., Keller, J., Lobell, J., ... Gergin, E. (1995, February). SWE, A Comprehensive Plasma Instrument for the Wind Spacecraft. *Space Sci. Rev.*, *71*, 55-77. doi: 10.1007/BF00751326

Parks, G. K., Lee, E., Fu, S. Y., Lin, N., Liu, Y., & Yang, Z. W. (2017, December). Shocks in collisionless plasmas. *Reviews of Modern Plasma Physics*, *1*(1), 1. doi: 10.1007/s41614-017-0003-4

Pollock, C., Moore, T., Jacques, A., Burch, J., Gliese, U., Saito, Y., ... others (2016, March). Fast Plasma Investigation for Magnetospheric Multiscale. *Space Sci. Rev.*, *199*, 331-406. doi: 10.1007/s11214-016-0245-4

Russell, C. T., Anderson, B. J., Baumjohann, W., Bromund, K. R., Dearborn, D., Fischer, D., ... Richter, I. (2016, March). The Magnetospheric Multiscale Magnetometers. *Space Sci. Rev.*, *199*, 189-256. doi: 10.1007/s11214-014-0057-3

Schwartz, S. J. (1998). Shock and Discontinuity Normals, Mach Numbers, and Related Parameters. *ISSI Scientific Reports Series*, *1*, 249-270.

Schwartz, S. J., Ergun, R., Kucharek, H., Wilson, L., Chen, L.-J., Goodrich, K., ... Strangeway, R. (2021, August). Evaluating the deHoffmann-Teller Cross-Shock Potential at Real Collisionless Shocks. *Journal of Geophysical Research (Space Physics)*, *126*(8), e29295. doi: 10.1029/2021JA029295

Schwartz, S. J., Henley, E., Mitchell, J., & Krasnoselskikh, V. (2011, Nov). Electron temperature gradient scale at collisionless shocks. *Phys. Rev. Lett.*, *107*, 215002. Retrieved from `https://link.aps.org/doi/10.1103/PhysRevLett.107.215002` doi: 10.1103/PhysRevLett.107.215002

Schwartz, S. J., Thomsen, M. F., Bame, S. J., & Stansberry, J. (1988). Electron heating and the potential jump across fast mode shocks. *Journal of Geophysical Research: Space Physics*, *93*(A11), 12923-12931. Retrieved from `https://agupubs.onlinelibrary.wiley.com/doi/abs/10.1029/JA093iA11p12923` doi: https://doi.org/10.1029/JA093iA11p12923

Sckopke, N., Paschmann, G., Bame, S. J., Gosling, J. T., & Russell, C. T. (1983, August). Evolution of ion distributions across the nearly perpendicular bow shock: specularly and non-specularly reflected-gyrating ions. *J. Geophys. Res.*, *88*(A8), 6121-6136. doi: 10.1029/JA088iA08p06121

Scudder, J. D. (1995, January). A review of the physics of electron heating at collisionless shocks. *Advances in Space Research*, *15*(8-9), 181-223. doi: 10.1016/0273-1177(94)00101-6

Shi, Q. Q., Shen, C., Dunlop, M. W., Pu, Z. Y., Zong, Q. G., Liu, Z. X., ... Balogh, A. (2006, April). Motion of observed structures calculated from multi-point magnetic field measurements: Application to Cluster. *Geophys. Res. Lett.*, *33*(8), L08109. doi: 10.1029/2005GL025073

Shi, Q. Q., Shen, C., Pu, Z. Y., Dunlop, M. W., Zong, Q. G., Zhang, H., ... Balogh, A. (2005, June). Dimensional analysis of observed structures using multipoint magnetic field measurements: Application to Cluster. *Geophys. Res. Lett.*, *32*(12), L12105. doi: 10.1029/2005GL022454

Vasko, I. Y., Mozer, F. S., Bale, S. D., & Artemyev, A. V. (2022). Ion-acoustic waves in a quasi-perpendicular earth's bow shock. *Geophys. Res. Lett.*, *49*(11), e2022GL098640. Retrieved from `https://agupubs.onlinelibrary.wiley.com/doi/abs/10.1029/2022GL098640` (e2022GL098640 2022GL098640) doi: https://doi.org/10.1029/2022GL098640

Vasko, I. Y., Mozer, F. S., Krasnoselskikh, V. V., Artemyev, A. V., Agapitov, O. V., Bale, S. D., ... Torbert, R. (2018, June). Solitary Waves Across Supercritical Quasi-Perpendicular Shocks. *Geophys. Res. Lett.*, *45*(12), 5809-5817. doi: 10.1029/2018GL077835

Vink, J., Broersen, S., Bykov, A., & Gabici, S. (2015, July). On the electron-ion temperature ratio established by collisionless shocks. *Astron. Astrophys.*, *579*, A13. doi: 10.1051/0004-6361/201424612

Vogt, J., Haaland, S., & Paschmann, G. (2011). Accuracy of multi-point boundary crossing time analysis. *Annales Geophysicae*, *29*(12), 2239–2252. Retrieved from `https://www.ann-geophys.net/29/2239/2011/` doi: 10.5194/angeo-29-2239-2011

Winske, D., & Quest, K. B. (1988, September). Magnetic field and density fluctuations at perpendicular supercritical collisionless shocks. *J. Geophys. Res.*, *93*, 9681-9693. doi: 10.1029/JA093iA09p09681